AD-A137 250 NUMERICAL MODELLING OF SEISMIC INTERFACE WAVES(U) 1/1
SACLANT ASW RESEARCH CENTRE LA SPEZIA (ITALY)
H SCHMIDT 15 DEC 83 SACLANTCEN-SM-169

UNCLASSIFIED F/G 8/11 NL

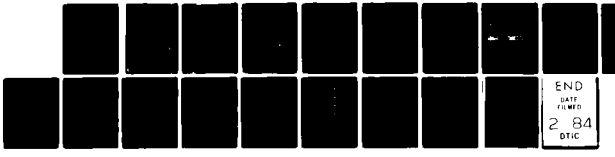

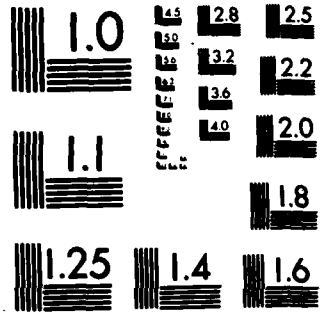

SACLANTCEN Memorandum
SM - 169

SACLANT ASW RESEARCH CENTRE MEMORANDUM

NUMERICAL MODELLING OF SEISMIC INTERFACE WAVES

by

Henrik SCHMIDT

15 DECEMBER 1983

NORTH ATLANTIC TREATY ORGANIZATION

LA SPEZIA, ITALY

Published by

SACLANTCEN MEMORANDUM SM-169

NORTH ATLANTIC TREATY ORGANIZATION

SACLANT ASW Research Centre
Viale San Bartolomeo 400, I-19026 San Bartolomeo (SP), Italy.

tel: national 0187 560940
international + 39 187 560940
telex: 271148 SACENT I

NUMERICAL MODELLING OF SEISMIC INTERFACE WAVES

by

Henrik Schmidt

15 December 1983

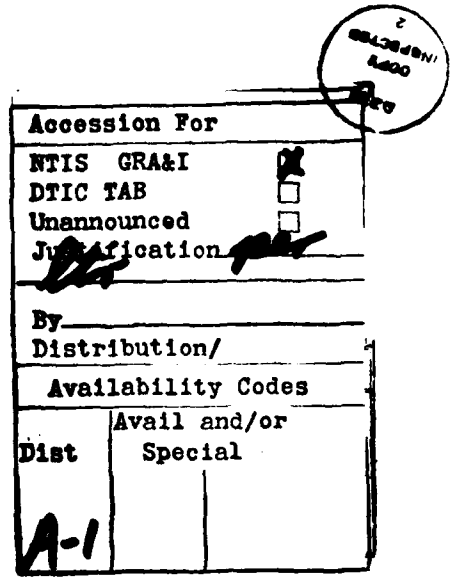

This memorandum has been prepared within the SACLANTCEN
Underwater Research Division as part of Project 19.

O.F. HASTRUP
Division Chief

TABLE OF CONTENTS

List of Figures

NUMERICAL MODELLING OF SEISMIC INTERFACE WAVES

by

Henrik Schmidt

ABSTRACT

A new numerical model based on the linear theory of elasticity and Marsh's approximation of the Hankel transform has been developed and used to model the excitation and propagation of interface waves in shallow-water sea-beds. Using realistic material parameters, the geometry and frequency-dependent propagation characteristics are analyzed and synthetic seismograms are produced. Basic properties of interface waves are discussed, and methods for direct evaluation of sea-bed properties from experimental results are proposed.

INTRODUCTION

The importance of the shear properties of the sea-bed for acoustic wave propagation in shallow water is well established <1>. Unfortunately the shear parameters are very difficult to isolate experimentally. They are, however, indirectly present through the properties of the measurable seismic interface waves, of which SACLANTCEN has made considerable experimental investigation in recent years <2,3>.

The mathematical model used in interpreting the experimental data has usually been based on the theory of elasticity. Since closed-form solutions cannot be obtained, numerical models based on the Thomson-Haskell technique have been used. The shear parameters are determined indirectly by fitting the model predictions to the experimental data by parametric studies. Due to the comprehensive computations needed at each frequency considered, only a few attempts have been made to determine the shear properties in this way, <4> for example. The present paper describes a new, fast, numerical model that has been used to clarify some of the basic principles involved in the propagation of interface waves in a simplified shallow-water environment. The influence of sediment thickness, frequency, and material properties is analyzed, and some guide lines are given for evaluating the shear properties directly from the experimental data.

1 THE MATHEMATICAL MODEL

The mathematical model is based on the assumption that the water column and the bottom consist of a series of range-independent layers. All materials are considered to be homogeneous and isotropic elastic continua with Lamé constants λ_n and μ_n and density ρ_n. The subscript refers to layer number n. The damping mechanisms are assumed to be linear viscoelastic.

A cylindrical coordinate system $\{r,\theta,z\}$ is introduced, with the z-axis going through the source and being positive downwards (Fig. 1). The representation of the cylindrical displacement components $\{u,v,w\}$ in terms of scalar potentials and the subsequent expression of these as Hankel transforms closely follows the presentation given by Schmidt and Krenk <5>; hence, only an outline will be given here. If body forces are neglected, the displacement equation of motion will be satisfied if the displacement components in layer n are expressed in terms of three scalar potentials $\{\Phi_n,\Psi_n,\Lambda_n\}$ as

$$u|_n = \frac{\partial \Phi_n}{\partial r} + \frac{1}{r}\frac{\partial \Psi_n}{\partial \theta} + \frac{\partial^2 \Lambda_n}{\partial e \partial z}$$

$$v|_n = \frac{1}{r}\frac{\partial \Phi_n}{\partial \theta} - \frac{\partial \Psi_n}{\partial r} + \frac{1}{r}\frac{\partial^2 \Lambda_n}{\partial \theta \partial z} \qquad \text{(Eq. 1)}$$

$$w|_n = \frac{\partial \phi_n}{\partial z} - \left(\frac{1}{r}\frac{\delta}{\partial r} r \frac{\delta}{\partial r} + \frac{1}{r^2}\frac{\partial^2}{\partial \theta^2}\right) \Lambda_n ,$$

where the potentials satisfy the wave equations

$$\left(\nabla^2 - \frac{1}{C_{Ln}^2}\frac{\partial^2}{\partial t^2}\right) \Phi_n = 0 \qquad \text{(Eq. 2)}$$

$$\left(\nabla^2 - \frac{1}{C_{Tn}^2}\frac{\partial^2}{\partial t^2}\right) (\Psi_n,\Lambda_n) = 0, \qquad \text{(Eq. 3)}$$

in which C_L and C_T are the velocities of the compressional and shear waves, respectively:

$$C_{Ln}^2 = \frac{\lambda_n + 2\mu_n}{\rho_n} \qquad \text{(Eq. 4)}$$

$$C_{Tn}^2 = \frac{\mu_n}{\rho_n} . \qquad \text{(Eq. 5)}$$

In the present case the field is asymmetric due to the positioning of the source on the axis, and the angular displacement v vanishes everywhere. It

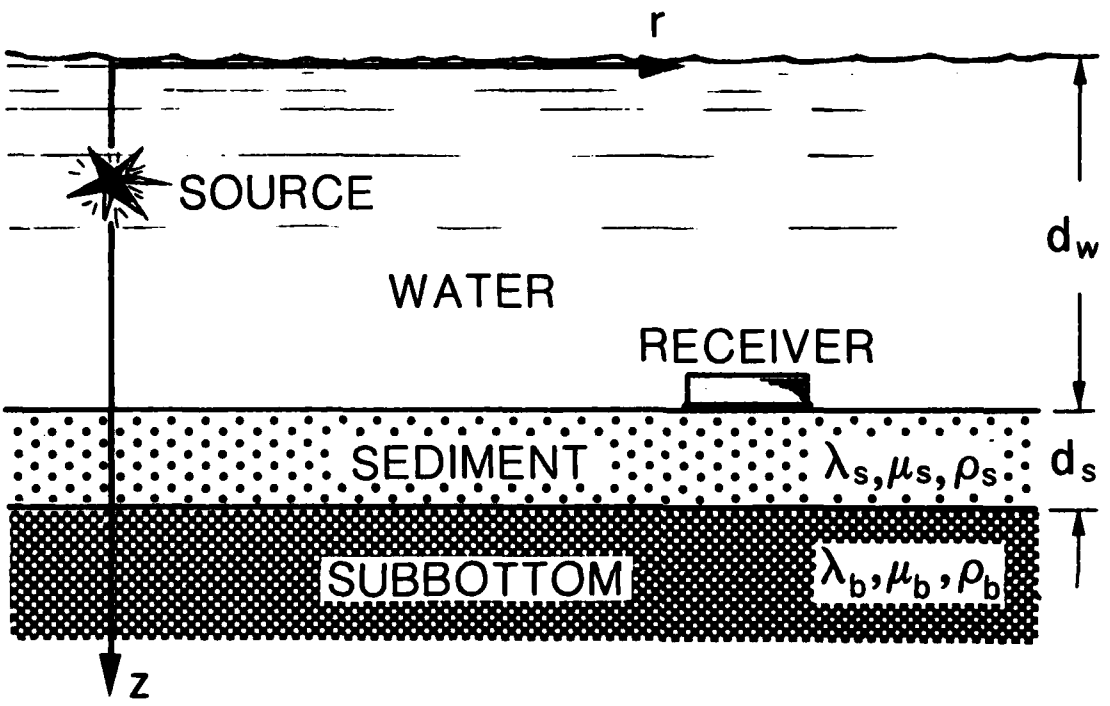

FIG. 1 SIMPLIFIED SEA-BED MODEL

is then clear from Eq. 1 that the potential Ψ_n must be constant and can be excluded.

In the following, only vibrations with angular frequency ω will be considered; displacements, stresses and potentials can then be expressed in complex form with the common factor $\exp(i\omega t)$. This factor will not be included in the following. The viscoelastic damping can now be accounted for by allowing the Lamé constants to be complex. After use of the Hankel transform on the wave equations, the following integral representations are obtained for the potentials:

$$\Phi_n(r,z) = \int_0^\infty \{A_n^-(s)e^{-z\alpha_n(s)} + A_n^+(s)e^{z\alpha_n(s)}\} J_0(rs)s\, ds \qquad \text{(Eq. 6)}$$

$$\Lambda_n(r,z) = \int_0^\infty \{B_n^-(s)e^{-z\beta_n(s)} + B_n^+(s)e^{z\beta_n(s)}\} J_0(rs)s\, ds, \qquad \text{(Eq. 7)}$$

where

J_m is the Bessel function of the first kind and order m.

A_n^-, A_n^+, B_n^- and B_n^+ are arbitrary functions in the horizontal wavenumber s,

$\alpha_n(s)$, $\beta_n(s)$ are defined as

$$\alpha_n(s) = \begin{cases} \sqrt{(s^2-h_n^2)}, & s > \mathrm{Re}\{h_n\} \\ i\sqrt{(h_n^2-s^2)}, & s < \mathrm{Re}\{h_n\} \end{cases} \qquad \text{(Eq. 8)}$$

$$\beta_n(s) = \begin{cases} \sqrt{(s^2-k_n^2)}, & s > \mathrm{Re}\{k_n\} \\ i\sqrt{(k_n^2-s^2)}, & s < \mathrm{Re}\{k_n\} \end{cases} \qquad \text{(Eq. 9)}$$

The wavenumbers h_n and k_n for the compressional and shear waves, respectively, are defined by

$$h_n^2 = \left(\frac{\omega}{C_{Ln}}\right)^2 = \frac{\omega^2\rho_n}{\lambda_n+2\mu_n} \qquad \text{(Eq. 10)}$$

$$k_n^2 = \left(\frac{\omega}{C_{Tn}}\right)^2 = \frac{\omega^2\rho_n}{\mu_n} \qquad \text{(Eq. 11)}$$

If Eqs. 6 and 7 are inserted into Eq. 1, the following expressions are obtained for the particle displacements:

$$w(r,z)\,|_n = \int_0^\infty \{-\alpha_n A_n^- e^{-z\alpha_n} + \alpha_n A_n^+ e^{z\alpha_n} + sB_n^- e^{-z\beta_n} + s B_n^+ e^{z\beta_n}\}\, s\, J_0(rs)ds, \qquad \text{(Eq. 12)}$$

$$u(r,z)\,|_n = \int_0^\infty \{-s A_n^- e^{-z\alpha_n} - s A_n^+ e^{z\alpha_n} + \beta_n B_n^- e^{-z\beta_n} - \beta_n B_n^+ e^{z\beta_n}\}\, s\, J_1(rs)ds. \qquad \text{(Eq. 13)}$$

The stress components involved in the boundary conditions follow, by Hooke's law:

$$\sigma_{zz}(r,z)\,|_n = \mu_n \int_0^\infty \{(2s^2-k^2)(A_n^- e^{-z\alpha_n} + A_n^+ e^{z\alpha_n}) + 2s\beta_n(-B_n^- e^{-z\beta_n} + B_n^+ e^{z\beta_n})\}\, s\, J_0(rs)ds, \qquad \text{(Eq. 14)}$$

$$\sigma_{rz}(r,z)\,|_n = \mu_n \int_0^\infty \{2s\alpha_n(A_n^- e^{-z\alpha_n} - A_n^+ e^{z\alpha_n}\} -(2s^2-k_n^2)(B_n^- e^{-z\beta_n} + B_n^+ e^{z\beta_n})\}\, s\, J_1(rs)\, ds. \qquad \text{(Eq. 15)}$$

In the case of a fluid layer the shear stiffness μ_n vanishes, and only the potential Φ_n is involved. The displacements follow directly from Eqs. 12 and 13 by setting B^-_n and B^+_n to zero. The shear stress is identically zero, whereas Eq. 14 has to be replaced by

$$\sigma_{zz}(r,z)\,|_n = -\lambda_n h^2 \int_0^\infty \{A_n^- e^{-z\alpha_n} + A_n^+ e^{ez\alpha_n}\}\, s\, J_0(rs)ds. \qquad \text{(Eq. 16)}$$

The source is assumed to be in layer number m at depth z_s. In the absence of boundaries, the field produced in layer m would be <6>:

$$\Phi_s(r,z) = \frac{iS_\omega}{4\pi} \int_0^\infty \frac{e^{-|\,z-z_s\,|\,\alpha_m}}{\alpha_m}\, s\, J_0(rs)ds\ , \qquad \text{(Eq. 17)}$$

$$A_s(r,z) \equiv 0\ , \qquad \text{(Eq. 18)}$$

where S_ω is the source strength. If Eq. 17 is inserted into Eq. 1, expressions similar to Eqs. 12 and 13 are obtained for the displacements,

and again Hooke's law yields expressions like Eqs. 14 and 15 for the stresses involved in the boundary conditions.

For each value of the range, r, the boundary conditions must be satisfied. In the upper and lower half-spaces the arbitrary functions, with superscript $^-$ and $^+$ respectively, must vanish due to the radiation condition. At each interface, w and σ_{zz} must be continuous, and at all solid/liquid interfaces the shear stresses must vanish. At solid/solid interfaces w, u, σ_{zz} and σ_{rz} must be continuous. This yields a linear system of equations in the arbitrary functions, to be satisfied at each horizontal wavenumber:

$$C_{ij}(s) \cdot A_j(s) = R_i(s) \ . \qquad \text{(Eq. 19)}$$

The vector $A_j(s)$ contains all the non-vanishing arbitrary functions, $C_{ij}(s)$ is the coefficient matrix, and $R_i(s)$ contains the contributions from the source. When the arbitrary functions are found, the field parameters at any depth and range can be obtained from the Hankel transforms (Eqs. 12 to 16) plus the source contributions (if the source and receiver are in the same layer).

An analytical solution of Eq. 19 is of course possible, leading to closed-form expressions for the arbitrary functions; but for more than a few layers this procedure would be inconvenient. Further, the Hankel transforms do not lead to closed-form solutions, but need numerical evaluation. Thus the most general way to proceed is to create a numerical model based directly on the system of equations (Eq. 19). Such a model is described in the next chapter.

2 THE NUMERICAL MODEL

The numerical evaluation of the Hankel transform necessitates a truncation and a discretization in the horizontal wavenumber s. As can be observed from Eqs. 17 and 8, the source terms decay exponentially for s going towards infinity. As the source terms form the right hand side of Eq. 19 the arbitrary functions will behave in the same way. It is therefore possible to truncate the integration interval in accordance with any accuracy demands. The fast-field technique introduced by Marsh <7> can then be used to evaluate the Hankel transforms.

The Bessel functions are expressed in terms of Hankel functions

$$J_m(rs) = \tfrac{1}{2}\left[H_m^{(1)}(rs) + H_m^{(2)}(rs) \right] \qquad \text{(Eq. 20)}$$

and each integral is split into two. As only outgoing waves are considered, the integrals involving $H_m^{(1)}(rs)$ are neglected, and $H_m^{(2)}(rs)$ is replaced by its asymptotic form

$$H_m^{(2)}(rs) \underset{rs\to\infty}{\sim} \left(\frac{2}{\pi rs}\right)^{\frac{1}{2}} e^{-i\left[rs-(m+\frac{1}{2})\frac{\pi}{2}\right]} \qquad \text{(Eq. 21)}$$

The integration over the truncated interval can now be performed by means of the fast fourier transform, and the actual field parameter is found at a number of ranges equal to the number of discrete wavenumbers considered.

DiNapoli and Deavenport <8> have compared Marsh's method to the technique introduced by Tsang, Brown, Kiang and Simmons <9>, which does not use the assymptotic form of the Hankel function and found significant differences only for very short ranges.

The kernels in the Hankel transforms are now needed only for a limited number of discrete values of s. Kutschale <10> and DiNapoli and Deavenport <8> used a Greens-function approach based on the Thomson-Haskell matrix method. However, their approach allows for only one source/receiver combination at a time. Here we solve Eq. 19 directly. The receiver depth is not involved in the equations and several receiver depths can therefore be handled with one solution. Further, the coefficient matrix does not include the source contribution, thus yielding the possibility of having several sources on the axis by simply adding their contributions to form the righthand side of Eq. 19.

The solution of Eq. 19 is the most critical point with respect to computation time, but if only the non-vanishing arbitrary functions are included and arranged properly, the coefficient matrix will be compact and of band form. The equations are then solved very efficiently by means of gaussian elimination with partial pivoting. In all cases treated, the total calculation time with this model was between 10 and 30% of what was used by Kutschale's model, with the biggest gain in cases with many layers. In cases with more than one source and receiver the gain is of course much more pronounced.

3 MODELLING OF SEISMIC WAVES

The numerical model has been used to analyze the propagation of low-frequency seismic waves in shallow-water sea-beds. In order not to obscure the basic principles, a simple two-layered model was chosen for the sea-bed, Fig. 1. Below the water column of depth d_w, a single sediment layer of thickness d_s covers a half-space of rock or rock-like material. The bottom materials used in the examples and their assumed properties are listed in Table 1. The complex Lamé constants are not given explicitly in the table. Instead, the compressional and shear velocities are shown, together with their respective dampings in decibels per wavelength.

TABLE 1

MATERIAL PROPERTIES

Material	Density ρ (g/cm^3)	Compressional Speed C_L(m/s)	Shear Speed C_T(m/s)	Compressional Attenuation γ_L(dB/Λ)	Shear Attenuation γ_T(dB/Λ)
Water	1.0	1500	-	-	-
Silt	1.8	1600	200	1.0	2.0
Sand	2.0	1800	600	0.7	1.5
Limestone	2.2	2250	1000	0.4	1.0
Basalt	2.6	5250	2500	0.2	0.5

Table 2 summarizes the test cases considered. As can be observed, the water depth is held constant in all cases. Soft and hard sediment layers of 50 m thickness are combined with two different sub-bottom materials in order to assess the effect of the material's properties. For one of the combinations the thickness of the sediment layer is varied. In the last test case the effect of a shear-speed gradient in the sediment layer is analyzed by subdividing the 50-m layer into ten homogeneous 5-m layers.

TABLE 2

TEST CASES

Test Case	Water Depth (m)	Sediment Thickness (m)	Sediment Material	Shear-Speed Gradient (m/s/m)	Sub-bottom Material
1	100	50	Silt	-	Limestone
2	100	30	Silt	-	Limestone
3	100	5	Silt	-	Limestone
4	100	50	Sand	-	Limestone
5	100	50	Silt	-	Basalt
6	100	50	Sand	-	Basalt
7	100	50	Silt	4	Limestone

In all cases a point source is placed in the middle of the water column at 50 m depth, and the vertical particle velocity at the top of the sediment layer is calculated using a pressure amplitude of 1Pa at a distance of 1 m

from the source. Only frequencies below and around the cut-off frequency for the first water mode are considered, which in the present case means frequencies below 10 Hz.

In the first test case a 50-m silt sediment layer covers a limestone subbottom. Figure 2 shows the modulus of the integrand in the Hankel transform of the vertical velocity at the top of the sediment layer for a frequency of 1.5 Hz. No water modes are present at this frequency, but two mode-like peaks can be observed at wavenumbers corresponding to phase velocities of 300 m/s (peak 1) and 840 m/s (peak 2). These peaks correspond to interface waves, and will be denoted the first and second interface mode, respectively. The first interface mode is best excited (highest amplitude), but it also has the highest damping (widest peak).

Figure 3 shows the corresponding vertical particle velocities at ranges up to 50 km. Due to the high damping of the first interface mode, its contribution is significant only for ranges shorter than 2 km, beyond which the second interface mode becomes dominant.

If the source is not of stationary type, but transient, the different velocities of the two interface modes will yield different arrival times, and the presence of the first interface mode will be measurable also at greater ranges. The phase and group velocities of the two interface modes have been calculated in the frequency band of interest, 0.1 to 10 Hz, with a resolution of 0.1 Hz. The results are shown in Fig. 4 together with an excitation measure, which somewhat arbitrarily has been chosen to be the particle velocity at 10 km range.

Since most of the general features of Fig. 4 exist in all test cases, a detailed interpretation will be given at this point. There is only one interface mode at frequencies below 1 Hz. It is slightly dispersive, with phase and group velocities approaching those of a Rayleigh wave on a limestone half-space. At 1 Hz a very sharp transition zone appears, where the velocities drop dramatically to values approaching those of a Scholte wave at a water/silt interface. At 1.8 Hz the group velocity reaches a minimum of 100 m/s, i.e. half the shear speed in silt. The second interface mode has a sharp cut-off at the transition frequency, and after a distinct minimum of the group velocity it appears as a logical continuation of the low-frequency part of the first interface mode. Above 2 Hz the excitation (solid line) of the second interface mode decreases due to the increased distance in terms of wavelengths of the source from the silt/limestone interface along which the second interface mode propagates. The sharp peak on the excitation curve around 4.5 Hz is the first propagation water mode.

The existence of mode transition zones is well known from the theory of vibration of elastic plates, Mindlin <11>, where they appear near the thickness-shear frequencies. These are the frequencies at which an infinite elastic plate can perform free shear vibrations with vanishing vertical displacements. Now consider the silt layer as an infinite elastic plate in welded contact with an infinite rigid half-space. The first thickness-shear frequency would then correspond to that of a free silt plate of the double thickness, <11>:

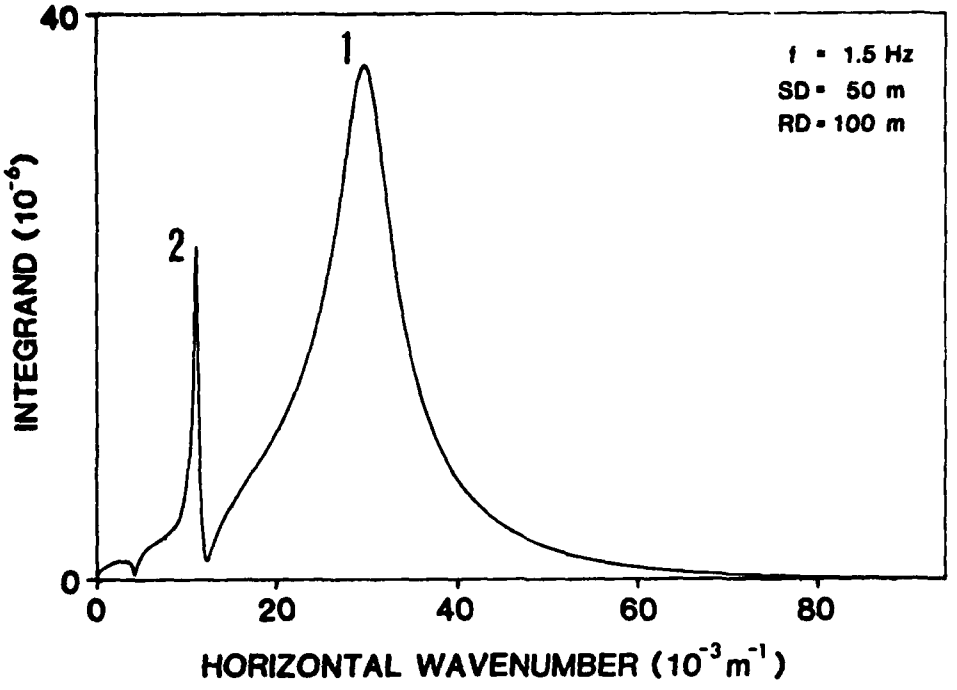

FIG. 2 INTEGRAND FOR VERTICAL PARTICLE VELOCITY AT 1.5 Hz
TEST CASE 1: 50 m SILT ON LIMESTONE

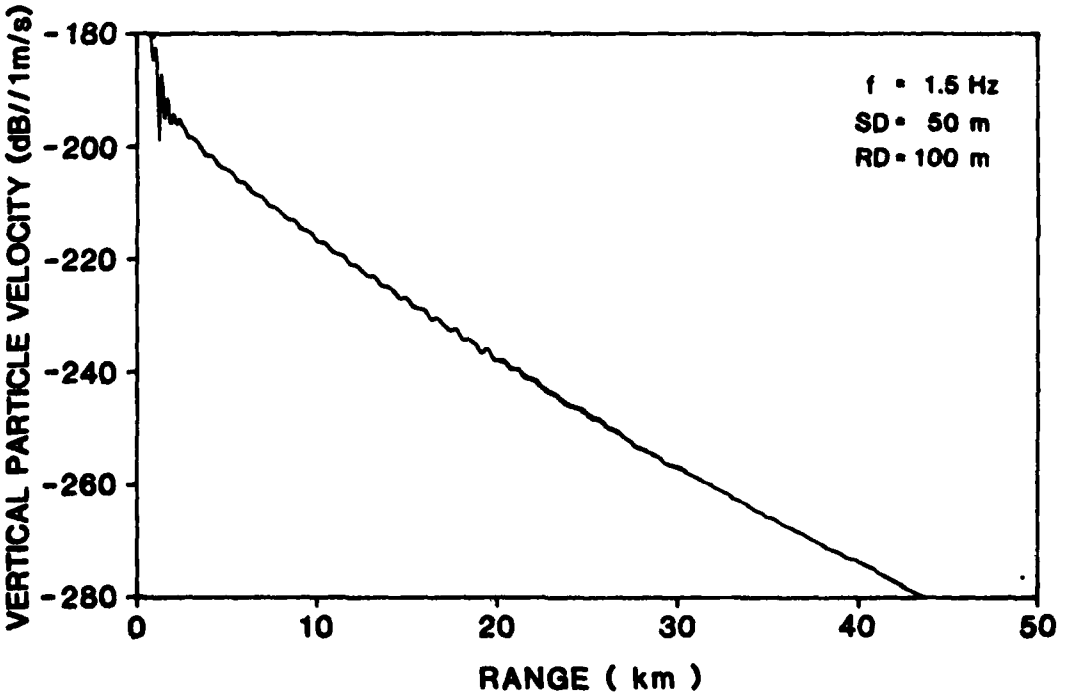

FIG. 3 VERTICAL PARTICLE VELOCITIES AT 1.5 Hz
TEST CASE 1: 50 m SILT ON LIMESTONE

$$f_{TS} = \frac{C_T}{4d_s} , \qquad \text{(Eq. 22)}$$

where C_T is the shear velocity and d_s is the thickness of the layer. If the parameters for silt are applied to Eq. 1, we obtain f_{TS} equal to 1 Hz, which is very close to the observed transition frequency in Fig. 4.

Since the transition frequency can be observed in experimental results, <3>, its correlation with the thickness-shear frequency could yield a direct method of determining the shear-wave velocity in a single sediment layer overlying a rigid half-space.

To summarize the general propagation characteristics for test case 1 (Fig. 4), the computed particle velocity at 10 km range is entirely associated with the first interface mode below the transition frequency (1 Hz). This interface mode is strongly related to a Rayleigh wave on a limestone half-space below 1 Hz, while it becomes an interface wave connected with the water/silt interface at frequencies above 1 Hz. In this frequency regime the second interface mode appears, and it is mainly related to the silt/limestone interface. Finally, the first water-borne mode appears at around 4.5 Hz.

In test case 2 (Fig. 5) the thickness of the silt layer has been reduced to 30 m. The general behaviour of the phase and group velocities is the same as in the former example, but the transition frequency is now at approximately 1.6 Hz, which is in good agreement with the computed thickness-shear frequency of 1.67 Hz. If the thickness of the silt layer is further reduced to 5 m, the thickness-shear frequency becomes 10 Hz, and no transition zone is present in the frequency range of interest.

In the fourth test case, the silt sediment is replaced by a sand layer of 50 m thickness. The transition zone is less sharp in this case (Fig. 6), probably due to the smaller difference between the stiffness of the sediment and the sub-bottom. In this case, the thickness-shear frequency is 3 Hz and the minimum group velocity is 400 m/s, or 67% of the shear speed. At the low-frequency end the velocities of the first interface mode again approach the velocity of a Rayleigh wave on the surface of a limestone half-space.

Silt and sand sediment layers (50 m) on basalt were also studied in order to analyze the effect of different sub-bottom materials. In the case of silt on basalt (Fig. 7) the low-frequency part of the first interface mode is excited only slightly, but the transition zone can again be observed near the thickness-shear frequency of 1 Hz. Above 1 Hz the dispersion curves are very similar to those obtained earlier for a sub-bottom of limestone (Fig. 4). In the case of sand on basalt (Fig. 8), the effect of the sub-bottom material is more pronounced. Compared with the case for limestone (Fig. 6), the basalt sub-bottom yields a much sharper transition zone near the thickness-shear frequency of the sand layer (3 Hz). The group velocity has a minimum of one-half of the shear speed in sand and the Rayleigh-wave behaviour at low frequencies can again be observed.

To investigate the effect of a shear gradient in the sediment layer, test case 1 (Fig. 4) was modified to include a gradient of 4 m/s/m in the silt layer. The result is given in Fig. 9. The main effect is seen to be a

FIGS. 4 to 9 EXCITATION AND DISPERSION CURVES

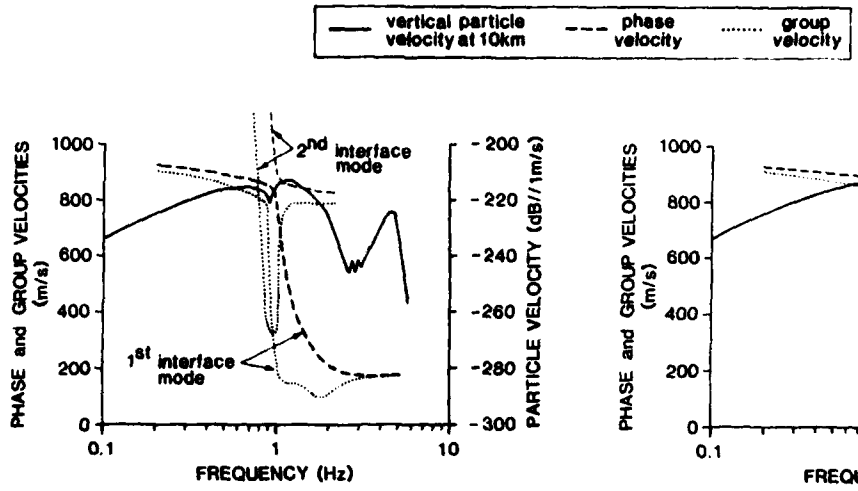

FIG. 4
TEST CASE 1: 50 m SILT ON LIMESTONE

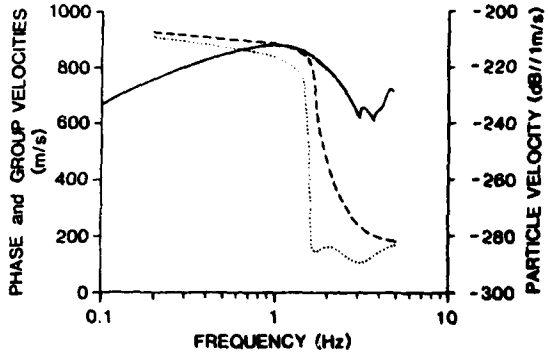

FIG. 5
TEST CASE 2: 30 m SILT ON LIMESTONE

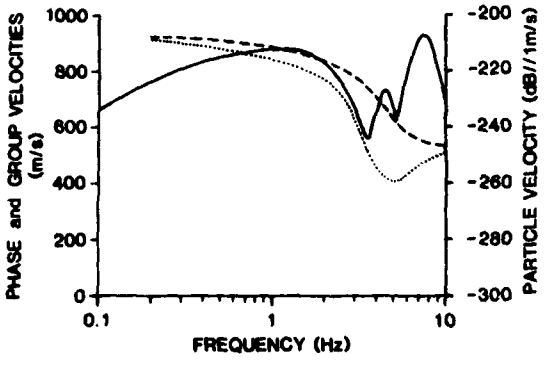

FIG. 6
TEST CASE 4: 50 m SAND ON LIMESTONE

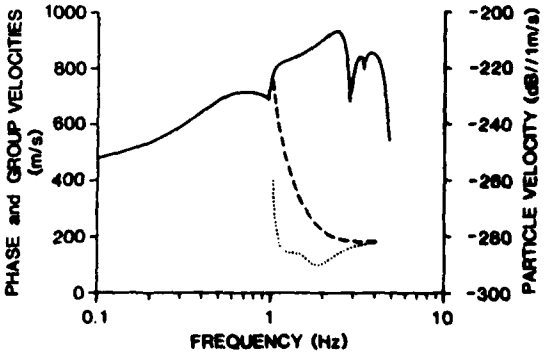

FIG. 7
TEST CASE 5: 50 m SILT ON BASALT

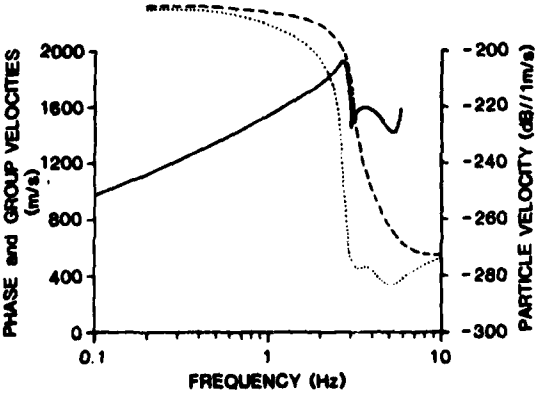

FIG. 8
TEST CASE 6: 50 m SAND ON BASALT

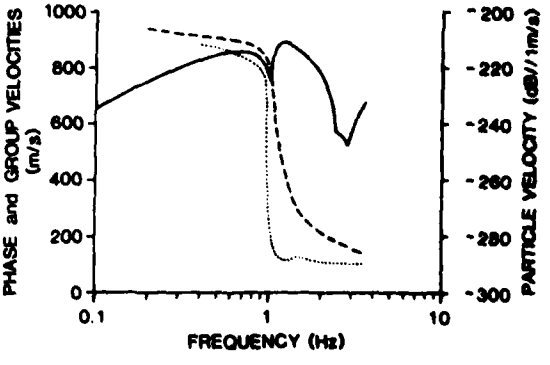

FIG. 9
TEST CASE 7: 50 m SILT WITH SHEAR SPEED GRADIENT ON LIMESTONE

change in the high-frequency limit of the dispersion curves for the first interface mode. Since the average shear-wave velocity is the same as in test case 1, the transition frequency is not affected. The effect on the high-frequency limit is not very surprising. The shorter the wavelength, the more dominant is the upper part of the sediment, yielding lower phase and group velocities. The almost non-dispersive nature of the first interface mode in this case is often seen in experimental data, <3>.

4 TIME SERIES

Although no attempt has been made to model experimental results, synthetic seismograms have been produced for two of the test cases in order to illustrate the time-domain effect of the features described above. The source is assumed to be half a sine wave of 1.5 Hz sent through an ideal 0.5 to 3.2 Hz band-pass filter. This frequency range has been chosen because it contains frequencies on both sides of the transition frequency for a silt sediment layer of 50 m thickness. The transfer functions were calculated to a resolution of 0.01 Hz and multiplied by the spectrum of the source. The time series were then created by means of the fast fourier transform at ranges of 1, 2, 3, 4 and 5 km.

Figure 10 shows the result for test case 1, i.e. a 50 m silt layer on a limestone half-space. The first weak arrival corresponds to a compressional wave in the limestone, whereas the first significant arrival corresponds to the Rayleigh wave velocity of the limestone (900 m/s). This arrival consists of the low-frequency parts of the first and second interface modes. A clear dispersion can be observed corresponding to the distinct minimum in the group velocity of the second interface mode in Fig. 4. The slow, highly damped wave, corresponding to the first interface mode above the transition frequency, propagates with group velocities between 100 and 180 m/s, again in good agreement with Fig. 4. At ranges greater than 4 km this arrival has negligible amplitude.

As described above, the low-frequency part of the first interface mode will not be significantly excited if the sub-bottom is basalt. The maximum excitation at 10 km range lies at 2.5 Hz (Fig. 7) and is due to a strong excitation of the second mode. These properties are also reflected in the synthetic seismograms (Fig. 11). The fastest arrival, apart from the weak compressional wave, has its major frequency content above 2 Hz and corresponds mainly to the high-frequency end of the second interface mode. The severe dispersion of the corresponding arrival in Fig. 10 is not present here, and the slow part of the first interface mode is well separated, travelling at group velocities between 100 and 200 m/s. The synthetic seismograms in Figs. 10 and 11 are, at least qualitatively, very similar to those observed during experiments, <2,3>.

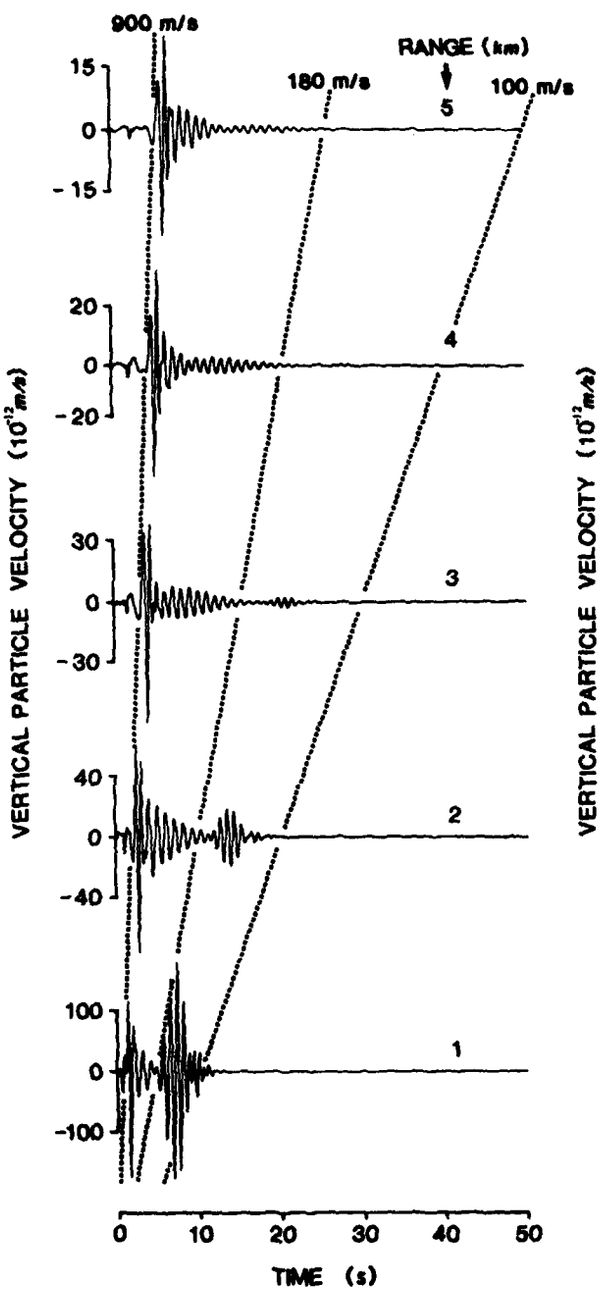

FIG. 10
STACKED SYNTHETIC SEISMOGRAMS
TEST CASE 1: 50 m SILT ON LIMESTONE

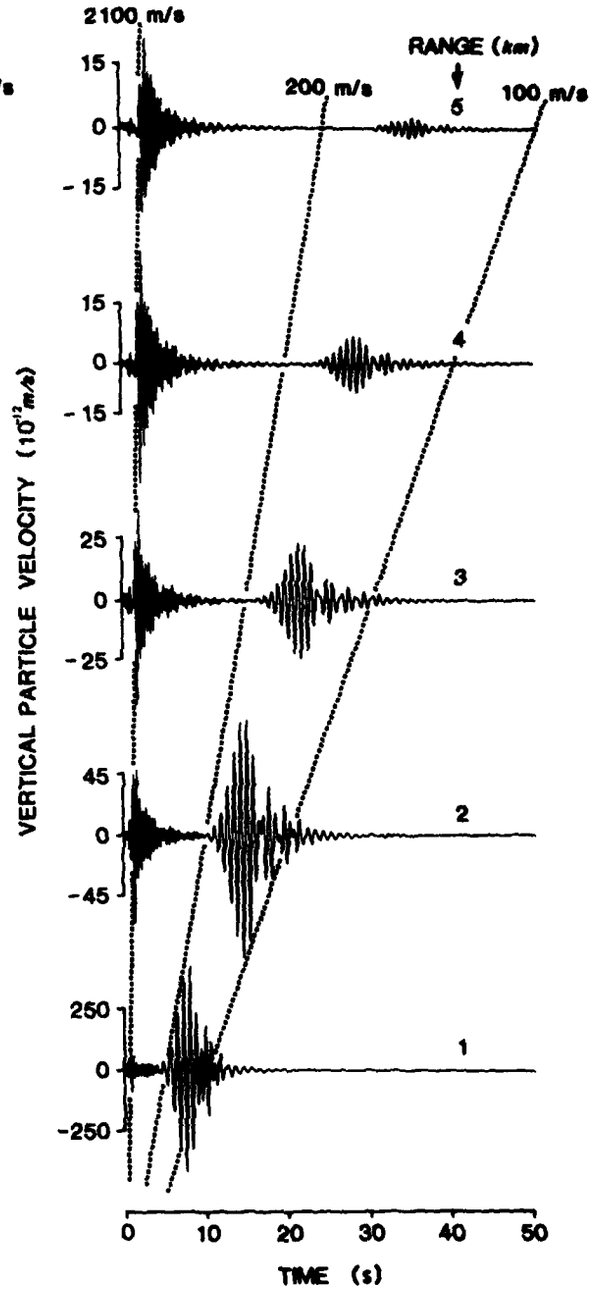

FIG. 11
STACKED SYNTHETIC SEISMOGRAMS
TEST CASE 5: 50 m SILT ON BASALT

CONCLUSIONS

A fast numerical model based on the linear theory of elasticity has been developed and used for the modelling of seismic waves in a shallow-water sea-bed. It is shown that a model of this type can be used to analyze the excitation and propagation of interface waves, reproducing many of the basic features observed during experiments, including the presence of a characteristic group-velocity transition zone.

One of the main prospects of the investigation of interface waves is the possibility of determining material properties that are not directly measurable, such as shear-wave velocities and dampings. Below the transition frequency, the propagation of the first interface mode is similar to that of a Rayleigh wave on a pure sub-bottom half-space. Its velocity and damping therefore yield information on the properties of the sub-bottom. The transition frequency is closely related to the first thickness-shear frequency of the sediment layer and is therefore a direct measure of the sediment shear speed. Above the transition frequency, the first interface mode is closely related to the water/sediment interface, and its properties can therefore be used to determine the properties of the sediment layer. The second interface mode, appearing above the transition frequency, is related to the sediment/sub-bottom interface and therefore contains coupled information on both media. If more than one sediment layer is present, several interface modes will appear, and the interpretation of the theoretical results can become quite complex.

REFERENCES

<1> AKAL, T. and JENSEN, F.B. Effects of the sea-bed on acoustic propagation. In: PACE, N.G., ed. Acoustics and the sea-bed. Proceedings of an Institute of Acoustics, Underwater Acoustics Group conference held at Bath University, Bath, U.K. 6-8 April, 1983. Bath, U.K., Bath University Press, 1983: pp 225-232.

<2> RAUCH, D. Experimental and theoretical studies of seismic interface waves in coastal waters. In: KUPERMAN, W.A. and JENSEN, F.B., eds. Bottom-interacting ocean acoustics. Proceedings of a conference held June 9-12, 1980 at the NATO SACLANT ASW Research Centre, La Spezia, Italy. New York, N.Y., Plenum Press, 1980: pp 307-327.

<3> RAUCH, D. and SCHMALFELDT, B. (1983). Ocean-bottom interface waves of the Stoneley/Scholte-type: properties, observations and possible use. In: PACE, N.G., ed. Acoustics and the sea-bed. Proceedings of an Institute of Acoustics, Underwater Acosutics Group conference held at Bath University, Bath, U.K., 6-8 April, 1983. Bath, U.K., Bath University Press, 1983: pp 307-316.

<4> ESSEN, H.H. Model computations for low-velocity surface waves on marine sediments. In: KUPERMAN, W.A. and JENSEN, F.B., eds. Bottom-interacting ocean acoustics. Proceedings of a conference held June 9-12, 1980 at the NATO SACLANT ASW Research Centre, La Spezia, Italy. New York, N.Y. Plenum Press, 1980: pp 299-305.

<5> SCHMIDT, H. and KRENK, S. Asymmetric vibrations of a circular elastic plate onan elastic half space. Internatinal Journal of Solids and Structures, 18, 1982: 91-105.

<6> EWING, W.M., JARDETZKY, W.S. and PRESS, F. Elastic Waves in Layered Media. New York, N.Y., McGraw-Hill, 1957.

<7> MARSH, H.W., SCHULKIN, M. and KNEALE, S.G. Scattering of underwater sound by the sea surface. Journal of the Acosutical Society of America 33, 1961: 334-340.

<8> DINAPOLI, F.R. and DEAVENPORT, R.L. Theoretical and numerical Green's function field solution in a plane multilayered medium. Journal of the Acoustical Society of America 67, 1980: 92-105.

<9> TSANG, L., BROWN, R., KONG, J.A. and SIMMONS, G. Numerical evaluation of electromagnetic fields due to dipole antennas in the presence of stratified media. Journal of Geophysical Research 1974: 2077-2080.

<10> KUTSCHALE, H.W. Rapid computation by wave theory of propagation loss in the Arctic Ocean, CU-8-73. Palisades, N.Y. Columbia University, Lamont Geological Observatory, 1973.

<11> MINDLIN, R.D. An introduction to the mathematical theory of vibration of elastic plates. Fort Monmouth, N.Y. U.S. Army Signal Corps Engineering Laboratories, 1955.

INITIAL DISTRIBUTION

MINISTRIES OF DEFENCE	Copies
MOD Belgium	2
DND Canada	10
CHOD Denmark	8
MOD France	8
MOD Germany	15
MOD Greece	11
MOD Italy	10
MOD Netherlands	12
CHOD Norway	10
MOD Portugal	2
MOD Turkey	5
MOD U.K.	20
SECDEF U.S.	68

NATO AUTHORITIES	Copies
Defence Planning Committee	3
NAMILCOM	2
SACLANT	10
SACLANTREPEUR	1
CINCWESTLANT/COMOCEANLANT	1
COMSTRIKFLTANT	1
COMIBERLANT	1
CINCEASTLANT	1
COMSUBACLANT	1
COMMAIREASTLANT	1
SACEUR	2
CINCNORTH	1
CINCSOUTH	1
COMNAVSOUTH	1
COMSTRIKFORSOUTH	1
COMEDCENT	1
COMMARAIRMED	1
CINCHAN	3

SCNR FOR SACLANTCEN	Copies
SCNR Belgium	1
SCNR Canada	1
SCNR Denmark	1
SCNR Germany	1
SCNR Greece	1
SCNR Italy	1
SCNR Netherlands	1
SCNR Norway	1
SCNR Portugal	1
SCNR Turkey	1
SCNR U.K.	1
SCNR U.S.	2
SECGEN Rep. SCNR	1
NAMILCOM Rep. SCNR	1

NATIONAL LIAISON OFFICERS	Copies
NLO Canada	1
NLO Denmark	1
NLO Germany	1
NLO Italy	1
NLO U.K.	1
NLO U.S.	1

NLR TO SACLANT	Copies
NLR Belgium	1
NLR Canada	1
NLR Denmark	1
NLR Germany	1
NLR Greece	1
NLR Italy	1
NLR Netherlands	1
NLR Norway	1
NLR Portugal	1
NLR Turkey	1
NLR UK	1
NLR US	1

Total initial distribution	247
SACLANTCEN Library	10
Stock	63
Total number of copies	320

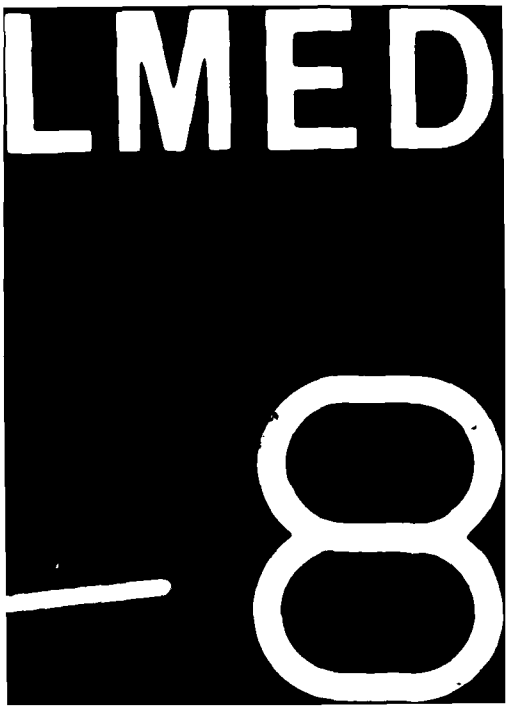
LMED
8